Journal of Marine Research, 74, 101–131, 2016

Western North Pacific Integrated Physical-Biogeochemical Ocean Observation Experiment (INBOX): Part 3. Mesoscale variability of dissolved oxygen concentrations observed by multiple floats during S1-INBOX

by Shinya Kouketsu[1,2], Ryuichiro Inoue[1], and Toshio Suga[1,3]

ABSTRACT

As part of the interdisciplinary project S1-INBOX (Western North Pacific Integrated Physical-Biogeochemical Ocean Observation Experiment conducted around the S1 biogeochemical mooring site), we used data from more than 18 floats and a biogeochemical mooring S1 (near 30° N, 145° E) to investigate temporal and spatial changes in the shallow oxygen maximum (SOM) associated with a mesoscale cyclonic eddy. On the northern edge of the cyclonic eddy, patches (linear dimensions of 20–40 km) with relatively high oxygen concentrations were observed around the SOM. The patterns of the oxygen concentrations reflected the fact that changes of the depths of the isopycnal surfaces were caused by small disturbances associated with the eddy structure along the eddy edge. The implication is that nutrient-rich water was supplied by upward isopycnal heaving at the edge of the eddy and contributed to the formation of the high-oxygen patches. As relatively high oxygen concentrations on the same isopycnal surfaces at greater depths were sometimes observed in the region downstream of the high-oxygen patches, we suggest that the patches were advected to the downstream region. The high-oxygen water seemed to extend into the eddy core from its edge. Ageostrophic secondary circulation around the edge of the eddy might have contributed to maintenance of the high oxygen concentrations in the eddy core, and these high oxygen concentrations may have been formed during spin-up of the eddy by heaving of isopycnal surfaces.

Keywords: meso-scale eddy, submeso-scale structure, biological activity, oxygen changes, shallow oxygen maximum

1. Introduction

In oligotrophic subtropical gyres, the dynamics associated with eddies play a crucial role in changing the biological environment because vertical and horizontal mesoscale and submesoscale dynamics associated with eddies can supply the euphotic zone with nutrient-rich water. McGillicuddy et al. (1998) suggested that isopycnal heaving associated with cyclonic

1. Research Institute for Global Change, Japan Agency for Marine-Earth Science and Technology (JAMSTEC), 2-15 Natsushima-cho, Yokosuka, Japan.
2. Corresponding author: ***e-mail: skouketsu@jamstec.go.jp***
3. Department of Geophysics, Graduate School of Science, Tohoku University, Sendai, Japan.

eddies made large contributions to annual nutrient budgets estimated in previous studies of the oligotrophic Sargasso Sea (Jenkins and Goldman 1985; Spitzer and Jenkins 1989; Sarmiento et al. 1990). Because the main thermocline of an anticyclonic eddy is deeper in the core than at the edge, it is difficult to bring nutrient-rich water to the surface in the core. However, an anticyclonic eddy that includes mode water in its core (a mode-water eddy) can be associated with conditions favorable for biological activity because such an eddy has a shallower seasonal isopycnal surface in its core (e.g., McGillicuddy et al. 1999). The mechanisms by which cold water is pumped up in the center of such eddies are important for the supply of nutrient-rich water to the euphotic zone, especially early in eddy development, because eddy intensification causes upwelling (Sweeney, McGillicuddy, and Buesseler 2003; Bibby et al. 2008). In addition, changes in the spatial characteristics of the wind stress attributable to surface currents associated with anticyclonic eddies can cause local Ekman pumping around the center of the eddy, which contributes to the uplifting of nutrient-rich water to the euphotic zone (e.g., Martin and Richards 2001). These effects are consistent with the observed chlorophyll *a* (chl. *a*) distribution and vertical velocity estimated with a tracer by Ledwell, McGillicuddy, and Anderson (2008) in a mode-water eddy in the northwestern Atlantic. Such changes in biological activity attributable to uplifting of nutrient-rich water from deeper layers can also be caused by sub-mesoscale disturbances around eddies (e.g., Lévy, Klein, and Treguier 2001; Calil and Richards 2010). Furthermore, the spatial pattern of chl. *a* estimated from satellite data can be strongly affected by advection caused by eddy-edge currents and the background, large-scale gradient of chl. *a* (Chelton et al. 2011). Siegel et al. (2011) characterized these four effects as "eddy pumping," "eddy-Ekman pumping," "sub-mesoscale pumping," and "eddy advection." They investigated the influence of these four effects on the pattern of chl. *a* concentrations estimated from satellite data around eddies and concluded that several of these mechanisms simultaneously affected the patterns.

During the Western North Pacific Integrated Physical-Biogeochemical Ocean Observation Experiment conducted around the S1 biogeochemical mooring site (S1-INBOX), we studied an area far from the Kuroshio Extension to avoid strong advection effects caused by the main current (Inoue, Suga et al. 2016; hereafter referred to as Part 1). In the recirculation gyre south of the Kuroshio Extension, where North Pacific Subtropical Mode Water (STMW) is frequently observed (e.g., Suga, Takei, and Hanawa 1997), Sukigara et al. (2011) have reported that strong vertical diffusion can supply enough nutrient-rich water from STMW to the seasonal pycnocline above to form shallow oxygen maxima, which have been observed by floats above STMW. Their estimate of diffusivity is consistent with previous results based on conservation of potential vorticity, in which it was assumed that horizontal advection was negligible at the center of the recirculation gyre (Qiu et al. 2006). However, estimates of horizontal variations based on observations by a single float are confounded by the assumption that the float tracks the same water column for several months. Since July 2011, we have deployed 18 floats with dissolved oxygen (DO) sensors around the S1 mooring site to document the spatial and temporal changes in the structure

of stratification and the distribution of oxygen around eddies and small disturbances. This study can serve as a pilot study for sustained future global biogeochemical observations, such as Oxygen-Argo or Bio-Argo (e.g., Gruber et al. 2007; Claustre et al. 2010), and contribute to their effective design and implementation.

This article is the third in a series of articles concerning the investigation of a cyclonic eddy located to the south of the S1 mooring from August to September 2011. In Part 1, we reported that based on a 2-month composite, the oxygen concentrations around the shallow oxygen maximum (SOM) were higher in the cyclonic eddy core than outside of the eddy. However, the temporal and spatial variances were not described in detail. In this article, we show detailed distributions of oxygen concentration in the euphotic zone around the eddy, focusing on small-scale (<100 km) disturbances as well as mesoscale (100–200 km) variations, which were revealed by the intensive float array observations. We first summarize the observation data and oxygen data quality used in this study (Section 2). In Section 3, we summarize properties of the cyclonic eddy and show the relationships between subsurface oxygen concentrations and isopycnal depths associated with the eddy and with small-scale, high-oxygen patches. We then compare the horizontal distributions of oxygen, chl. *a*, and vertical velocity. The effect of disturbances associated with small-scale, high-oxygen patches around the edge of the eddy are discussed in Section 4. We summarize the results in Section 5. The methods used to estimate vertical velocity fields are explained in the Appendix. The chronology is based on assignment of time intervals in days since January 1, 2011 (YDAYs).

2. Data

a. Observation data

We used temperature, salinity, and oxygen profiles from the surface to 2,000 dbar obtained by 18 Argo-type floats, which sent the profiles and the locations automatically to a satellite every 2 days. The floats were deployed around the S1 mooring site (see details in Part 1). To characterize the nutrient conditions, we used the nitrate concentrations in sample bottles at the beginning of the float array observations. To compare the observations at S1 with the float array observations, we used the salinity, temperature, oxygen, chl. *a*, and potential oxygen production observations made with the underwater profiling buoy system (Inoue, Honda et al. 2016; hereafter referred to as Part 2).

We used $1/3^\circ \times 1/3^\circ$ gridded sea surface height anomaly (SSHA) data to characterize surface current fields associated with eddies. The data were produced by the Segment Sol Multimissions d'Altimétrie d'Orbitographie et de Localisation Précise/Data Unification and Altimeter Combination System and distributed by the Archiving, Validation and Interpretation of Satellites Oceanographic Data, with support from the Centre National d'Etudes Spatiales. The weekly composites of surface chl. *a* on $1/3^\circ \times 1/3^\circ$ grids were calculated from 8 km × 8 km daily composite products provided by the NASA's Goddard Space Flight Center (McClain, Feldman, and Hooker 2004).

b. Quality of oxygen measurements by the floats and underwater profiling buoy system

Oxygen sensors on the floats were calibrated using the RINKO (JFE Advantech Co. Ltd., Nishinomiya, Japan) DO sensor that was deployed as part of ship-based conductivity-temperature-depth (CTD) casts following the calibration method proposed by Uchida et al. (2008). The RINKO was calibrated with the oxygen data from the bottle water samples: the standard deviation of the differences between RINKO and bottle samples was 2 μmol kg^{-1} To calibrate the oxygen float measurements, we selected the nearest profile for each float from the Shipboard CTD-RINKO station (the distances were 5–45 km) within 4 days from the day when the station was occupied. After the adjustments for the float measurements, the standard deviation of the differences between the float and RINKO measurements was 3 μmol kg^{-1} (Part 1). The comparability of oxygen measurements between floats was not determined. We evaluated oxygen measurement uncertainty and drifts based on the differences in oxygen concentrations between two floats that we assumed were monitoring similar water masses (Fig. 1). For the purposes of this comparison, we selected pairs of casts by different floats that were within 0.05° latitude and longitude of each other. We then compared oxygen values measured at the same depths with small temperature and salinity differences ($<$0.005°C and $<$0.005, respectively) in the casts. Although the range to select the data was narrow, 425 pairs of casts, including all 18 floats with the oxygen sensor, and more than a thousand oxygen concentration measurements were available for the comparison. The standard deviation of the differences within pairs (Fig. 1a) was 1.8 μmol kg^{-1}; there were no significant changes in the differences over time (Fig. 1b). We thus assumed that temporal and spatial changes greater than approximately 3 μmol kg^{-1} could be detected by this float array, which was smaller than the temporal and spatial variability around the eddy (5 μmol kg^{-1}) discussed in this article.

The oxygen measurements by the underwater profiling buoy system (O_{PBS}) mooring (see Part 2) were calibrated (O_{corr}) with the simple linear equation ($O_{corr} \approx O_{FLT} = 0.54O_{PBS} + 91$) using float measurements (O_{FLT}) with a least squares fitting. In the resulting profiles, the SOM values from the profiling buoy were close to the ones (approximately 220 μmol kg^{-1}) from the floats (shown in Part 2). The detailed calibration methods are described in Part 2.

3. Results

a. History of the cyclonic eddy

The cyclonic eddy in the observation domain was defined by a local minimum of the SSHA in the region of positive vorticity estimated with the SSHA data (Fig. 2). The eddy was identified by the closed SSHA contours located around 28.5° N, 145° E, south of the S1 mooring on YDAY 165 in 2011 (Fig. 2a). After a small positive vorticity anomaly at 27.5° N, 147.5° E on YDAY 165 moved to the west and merged with an eddy to the south of the S1 mooring (Fig. 2b and c), the eddy moved to the north (Fig. 2d). At the beginning of the float observations (YDAY 207), the cyclonic eddy arrived at 29° N, 145.5° E. The

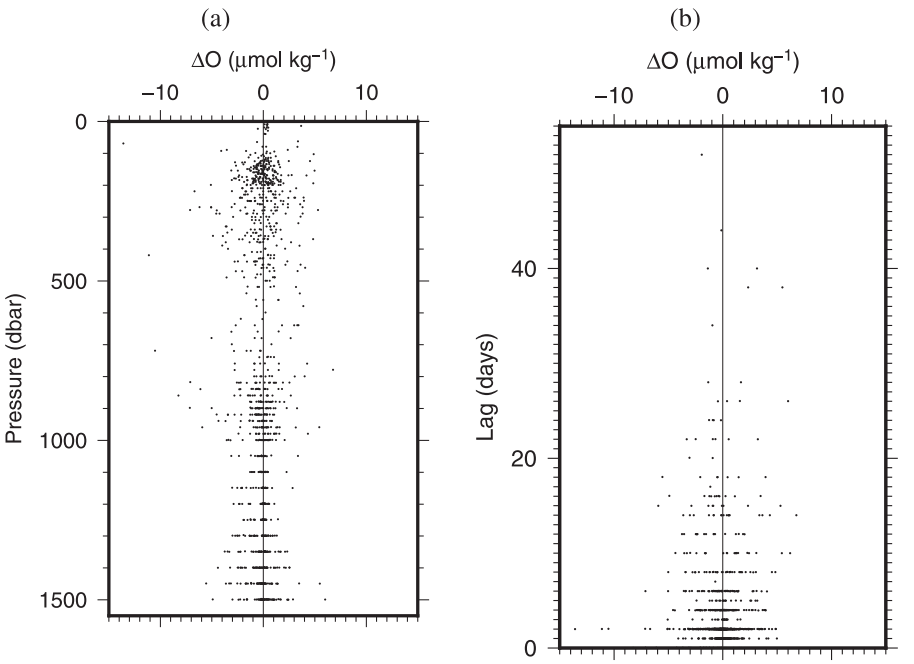

Figure 1. Oxygen differences between observations by pairs of proximate floats, shown by pressure (a) and temporal lag (b). The pairs of observations were selected so that the distance between the two floats was within 0.05° of latitude and longitude, and differences of temperature and salinity at the same level were within 0.005°C and 0.005, respectively.

vorticity strength and location of the cyclonic eddy remained more or less constant before YDAY 249 (Fig. 2e–g). After YDAY 249, the three positive vorticity maxima along 28.5° N seemed to merge, and the cyclonic eddy broadened and weakened (Fig. 2g and h).

b. Oxygen and isopycnal distributions corresponding to the eddy

Floats recorded the profiles of temperature, salinity, and oxygen around the eddy (Fig. 3). As described in Part 1, by using composites of the float observations, we observed SOMs with relatively higher oxygen concentrations around 24.0 potential density (σ_θ) near the eddy core. In the eddy core, nutrient-rich water could be uplifted associated with isopycnal surface upward heaving in the eddy core, and the shallower isopycnal could keep favorable light conditions for phytoplankton. The higher oxygen concentration in these SOMs might have been caused by such an environment in the eddy core. To show the radial structures corresponding to the eddy and their variations, we compared the oxygen concentrations and isopycnal depths around and below SOMs with respect to the SSHA (Fig. 3) for YDAYs 207–272. To remove the effect of temporal changes of SSHA at the eddy center, we used the differences of SSHA (dSSHA) from the eddy center defined as the local minimum

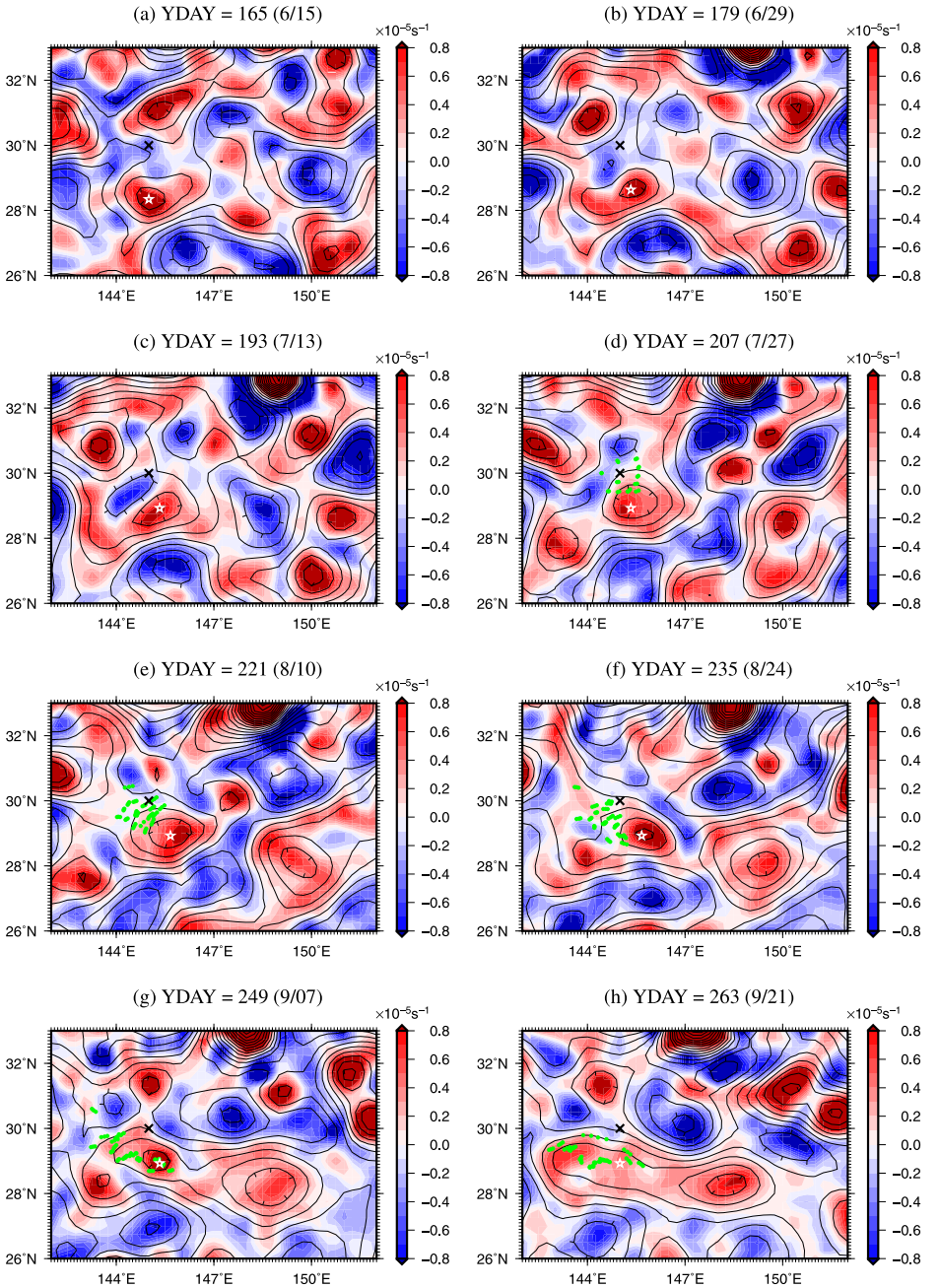

Figure 2. Relative vorticity (colored shading) calculated from sea surface height anomaly (SSHA) aroud YDAY = 165 (a), YDAY = 179 (b), YDAY = 193 (c), YDAY = 207 (d), YDAY = 221 (e), YDAY = 235 (f), YDAY = 249 (g), and YADY = 263 (h). Contours show SSHA values (the contour interval is 5 cm). Float observations are shown by green dots. The white star denotes the target eddy center in this study, which is defined by SSHA local minima. The black X denotes the location of the S1 mooring station. YDAY, time interval in days since January 1, 2011.

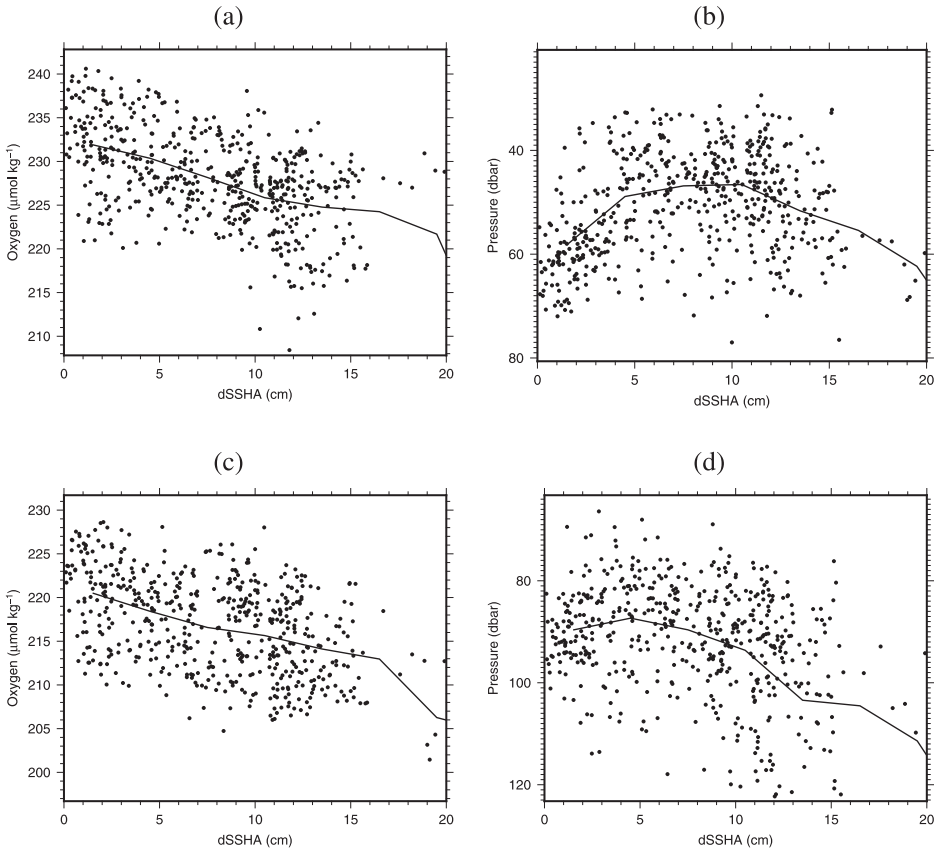

Figure 3. Oxygen concentration, at 24.0σ_θ (a) and at 24.8σ_θ (c), and isopycnal surface depths, at 24.0σ_θ (b) and at 24.8σ_θ (b), versus the SSHA difference from the eddy center (dSSHA). Thick black lines are the 3 cm dSSHA bin–averaged values for the oxygen concentrations and the depths, respectively. σ_θ, potential density; SSHA, sea surface height anomaly.

of SSHA. The higher oxygen concentrations on isopycnal surfaces were generally near the eddy center (Fig. 3a and c). However, the 24.0σ_θ isopycnal surface depths were not constantly shallower toward the eddy core than outside of the eddy (Fig. 3b) because of temporal changes in eddy strength as discussed in Part 1. The isopycnal surfaces in the eddy core were clearly shallower than those outside of the eddy below the SOMs (e.g., 24.8σ_θ; Fig. 3d); the correlations of isopycnal depths and oxygen to dSSHA on 24.8σ_θ (Fig. 3c and d) were approximately 0.4 and –0.5, respectively. However, the variability in each dSSHA bin was as large as the differences of bin-averaged oxygen concentrations and isopycnal surface depths between the inside and outside of the eddy core (e.g., 10 μmol kg^{-1} and 10 dbar differences at dSSHA = 1.5 cm and dSSHA = 11.5 cm, respectively; see Fig. 3).

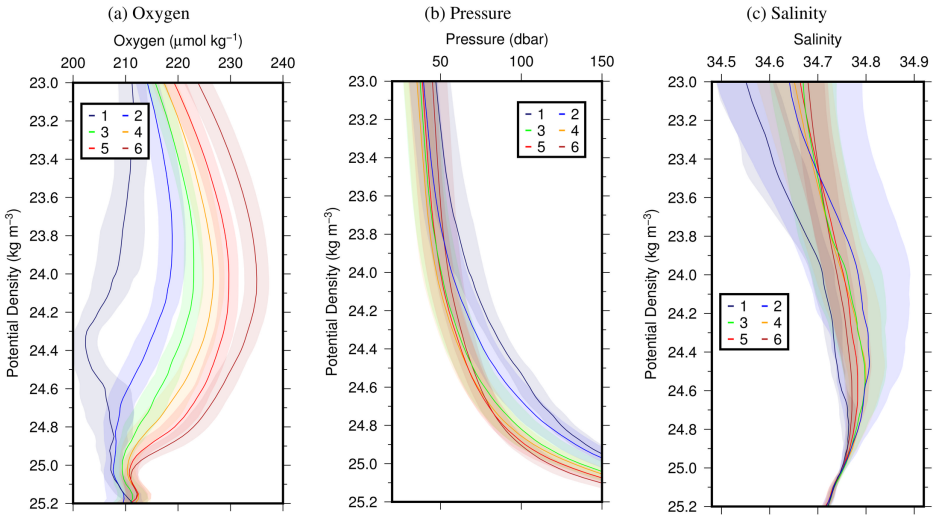

Figure 4. Oxygen (a), pressure (b), and salinity (c) for each group determined by the cluster analysis for the oxygen concentrations on potential density (σ_θ) surfaces from 23.0 kg m^{-3} to 25.2 kg m^{-3} at intervals of 0.1 kg m^{-3}. The colored shading denotes the standard deviation on the isopycnals for each group.

Thus, to elucidate such changes comparable to those across typical eddy structures, we focused on the horizontal distribution and temporal variability of oxygen concentrations.

c. Grouping water properties

To objectively elucidate the representative relationship around the SOM between vertical oxygen profiles and the cyclonic eddy in the horizontal distributions, we first used cluster analysis (Ward 1963) based on similarity between oxygen concentration profiles to divide all oxygen profiles into six groups (Fig. 4). Squared Euclidean distances, which are used to determine dissimilarity between observations in the cluster analysis, were defined to be the sum of the squares of the oxygen concentration differences on σ_θ surfaces. The oxygen concentration differences were calculated from 23.0 kg m^{-3} (corresponding to approximately 40 dbar) to 25.2 kg m^{-3} (160–230 dbar) at intervals of 0.1 kg m^{-3}. The range of density corresponded to the region between the base of the mixed layer (e.g., fig. 16c–e in Part 1) and the layer below the bottom of the euphotic zone, which was chosen to avoid strong diapycnal mixing attributable to surface forcing and to focus on changes of oxygen concentrations attributable to phytoplankton activity and subsurface physical processes. The depth of the euphotic zone was estimated from satellite images with the method shown by Morel and Berthon (1989) to be approximately 100 m; it did not change spatially (e.g., Fig. 5) or temporally (not shown).

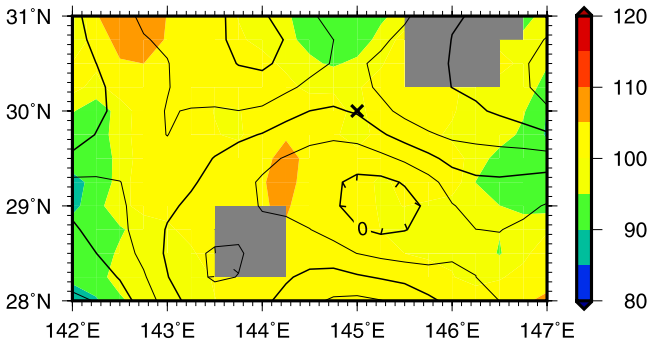

Figure 5. Euphotic layer thickness (m; colored shading) distribution estimated from satellite chlorophyll *a* (Morel and Berthon 1989) for YDAY = 249 around the observation domain in this study. Contours show SSHA values (cm; the contour interval is 5 cm). The black X denotes the location of the S1 mooring station. SSHA, sea surface height anomaly; YDAY, time interval in days since January 1, 2011.

The oxygen concentrations near the SOM, which was observed at approximately 40 m depth, differed between six groups because oxygen variability was high around the SOM. The SOM also corresponded to a local minimum of the negative apparent oxygen utilization (AOU; fig. 10 in Part 1) as a function of depth. Such a negative local minimum associated with the SOM could not be formed by simple advection of oxygen. As AOU is generally close to zero (and oxygen concentration is near saturation) in the wintertime mixed layer, which deepens down to 200 m in this region, and AOU increases (as oxygen concentration decreases) in association with remineralization after the winter, AOU around the SOM below the mixed layer should be positive or close to zero without phytoplankton activity. Thus, the SOM reflected oxygen production and presumably nutrient uptake by subsurface phytoplankton. The oxygen concentration of the SOM of group 6 was highest (approximately 240 μmol kg^{-1}), and that of group 2 was lowest (approximately 220 μmol kg^{-1}). These SOMs were observed at potential densities of 23.6–24.5 kg m^{-3}, right at the top of the nutricline that was observed at the beginning of the float observations (Fig. 6). There was no clear SOM in group 1 (Fig. 4a). The standard deviations of the salinities of each group were large at the SOMs (Fig. 4c), suggesting that waters from various sources had been advected to the SOM layers. Below the SOMs to the bottom of the euphotic zone (around $\sigma_\theta = 25.0$), the differences in oxygen concentrations among groups 2–6 were smaller on the denser isopycnal surfaces (Fig. 4), where nitrate increased rapidly with depth (Fig. 6); there, the high nitrate concentrations imply that photosynthetic production of oxygen by the phytoplankton was not nutrient limited.

Noteworthy is that below the SOM ($\approx$50 dbar), nitrate could be detected in all of the casts, although the standard deviations of the nitrate concentrations averaged on the isopycnal surfaces (50–150 dbar) were large (Fig. 6). Furthermore, in these layers near the bottom

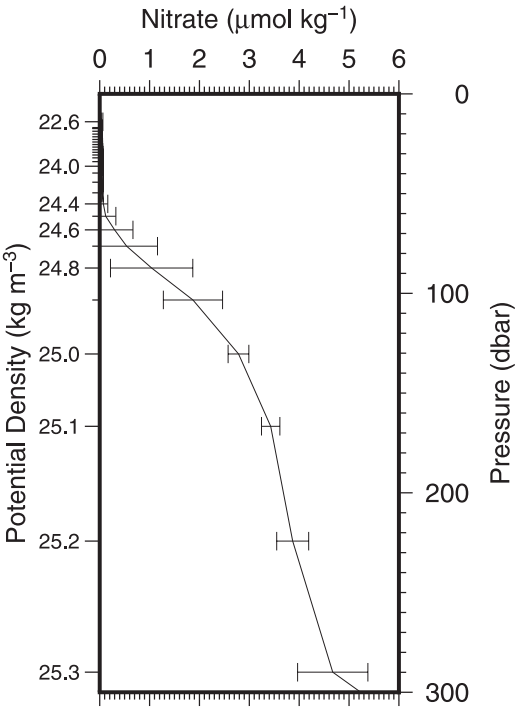

Figure 6. Nitrate (μmol kg^{-1}) profile averaged on isopycnal surfaces (left ordinate) with the profiles obtained during the MR11-05 cruise. The bars show the standard deviations of nitrate concentrations on each isopycnal surface. The right ordinate shows the average pressure level for each isopycnal surface.

of the euphotic zone, the mean isopycnal surfaces were shallower in groups 3, 4, 5, and 6 than in the analogous surfaces in groups 1 and 2. Because these isopycnal surfaces were near the bottom of the euphotic zone, this result indicates that uplifting of nutrient-rich waters contributed to the formation of high oxygen concentrations, as seen in groups 5 and 6. Below the euphotic zone, the local maximum of DO of 215 μmol kg^{-1} at $\sigma_\theta = 25.2$ kg m^{-3} corresponded to STMW.

d. Horizontal distributions of groups

As the variations in oxygen concentration in each SSHA bin (Fig. 3) were so large, we examined the longitude-latitude distributions of oxygen concentrations around the SOM and their temporal changes for two periods in detail with the objectively classified groups in the previous section (Fig. 4). On YDAYs 207–242 (late July through August), the floats were located mainly in the northwestern corner of the cyclonic eddy; each oxygen profile group was distributed across SSHA contours (Fig. 7a and b). Of the profiles sampled around

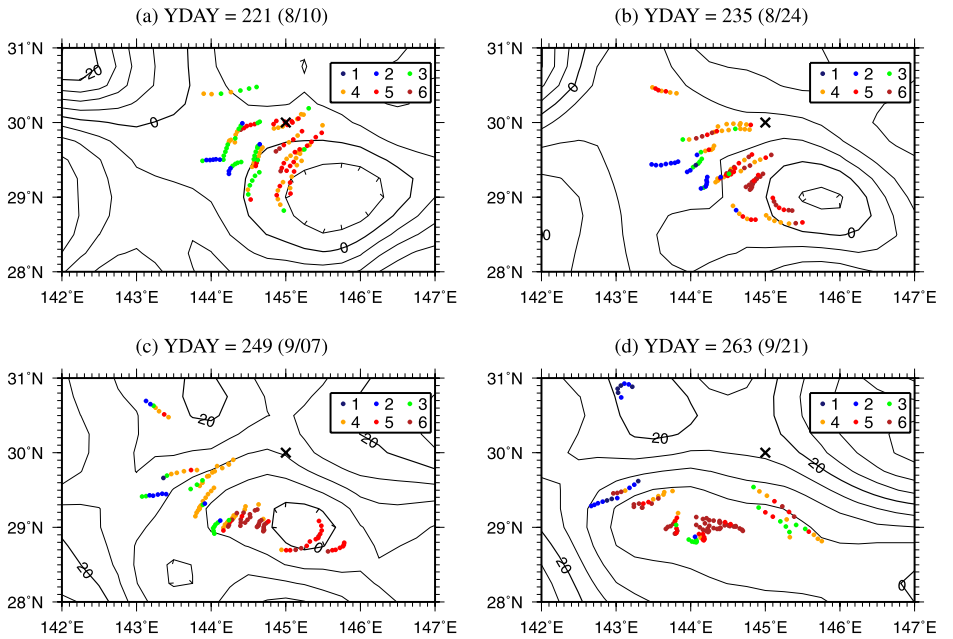

Figure 7. Distribution of the oxygen profile groups during a period of 2 weeks around YDAY = 221 (a), YDAY = 235 (b), YDAY = 249 (c), and YDAY = 263 (d). The YDAYs (dates) are the middle dates for the period. The colors of the groups are the same as those shown in Figure 4. Contours show the SSHA (cm). The black X denotes the location of the S1 mooring station. SSHA, sea surface height anomaly; YDAY, time interval in days since January 1, 2011.

YDAY 221, most were classified into groups 3, 4, and 5. Group 4 and 5 profiles, in particular, were both inside and outside of the eddy core, defined by SSHA of 0 cm (the closed contour in Fig. 7a). In contrast, most group 3 profiles, in which a relatively low oxygen concentration was observed at the SOM (Fig. 7a), were outside the eddy core. By around YDAY 235, the differences in the profiles along the SSHA contours (e.g., the 5 cm contour) had increased (Fig. 7b) Group 3 had become less prevalent, and clear, narrow bands (widths ≈20–40 km) of group 2 profiles (from 29.5° N, 143.6° E to 29.0° N, 144.3° E) and group 6 profiles (from 30.0° N, 144.2° E to 29.0° N, 145.0° E) were observed. High oxygen concentrations in the SOMs (corresponding to groups 4, 5, and 6) were therefore not always observed near the eddy core (low SSHA), whereas oxygen concentrations below the SOM could be associated with local changes of isopycnal depths along the eddy edge as the mean isopycnal depths in group 6 with high oxygen concentrations were shallower than those in group 2 with low oxygen concentrations below the SOM (see Fig. 4a and b). During this period, the variations of salinity around the SOM were large (around the 24.0σ_θ isopycnal surface in Fig. 8a and b). As the floats were collecting data from around the eddy edge (Fig. 7a and b), the large variations were attributable to the horizontal transport of different water masses by

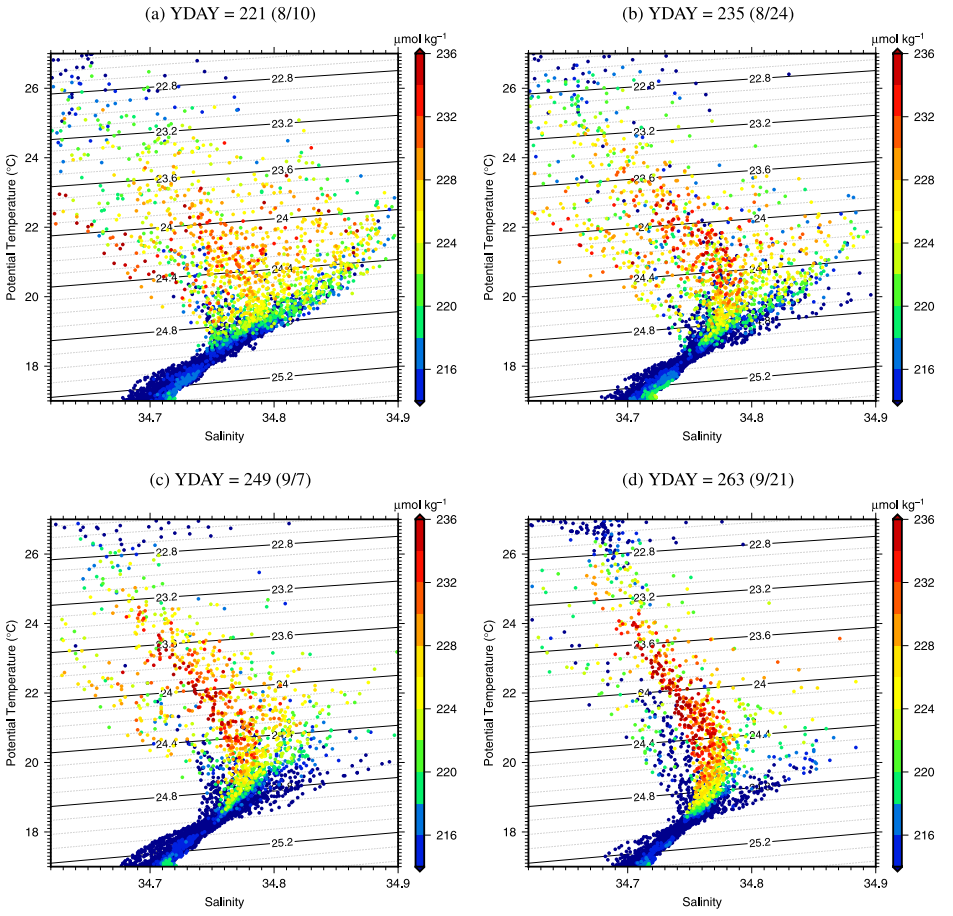

Figure 8. Temperature-salinity diagrams for oxygen (color) over four 2-week periods around YDAY = 221 (a), YDAY = 235 (b), YDAY = 249 (c), and YDAY = 263 (d). The YDAYs (dates) are the middle dates for the composite period. YDAY, time interval in days since January 1, 2011.

the eddy edge currents; these variations resulted in the large standard deviations of salinity in all groups (Fig. 4c) during all analysis periods.

In contrast, during the second period (YDAYs 243–272, September), there were clear relationships between the oxygen profiles and the SSHA. The pattern of narrow bands along SSHA contours (e.g., along the 5–10 cm contours in Fig 7c and d) was unclear because only a few floats recorded measurements at the eddy edge during this period. Almost all the profiles with high oxygen concentrations in the SOM (groups 5 and 6) were observed only in the eddy cores (in the SSHA 5 cm closed contour in Fig. 7c and d), where the uplifted isopycnal surfaces brought nutrient-rich water into the euphotic zone and thereby

created conditions favorable for phytoplankton growth. The variations in salinity around the SOM (around the 24.0σ_θ isopycnal surface; Fig. 8c and d) were smaller than those during the earlier period (Fig. 8a and b), and the relatively high oxygen concentrations in the SOMs at salinities of 34.74–34.78 were higher than those during the first period. This pattern suggests that the water properties were relatively uniform in the eddy core, which had not been strongly affected by horizontal advection. There were, however, small spatial variations: around YDAY 263, the oxygen concentrations in the SOM were higher in the eastern part of the cyclonic eddy (around 145.2° E) than in the western part (143° E) (Fig. 7d).

e. Relationship between depths of isopycnal surfaces and oxygen concentrations

The cluster analysis revealed that the isopycnal depths of the groups with higher oxygen concentrations in the SOM were shallower than those with lower oxygen concentrations (Fig. 4a and b). The high oxygen concentrations around the SOM may be related to shallow isopycnals associated with not only the eddy structures (Fig. 3) but also small disturbances around the eddy (e.g., Fig. 7), which could bring nutrient-rich water into the euphotic zone. Furthermore, the strength of such relationships between the isopycnal depths and oxygen concentrations differed between the SOM and below it (Fig. 4a and b).

To further quantify this difference, we used empirical orthogonal function (EOF) analysis (also known as principal component analysis) to explore the relationship between the depth of isopycnal surfaces and oxygen concentrations on 24.0σ_θ (at the SOM) and 24.8σ_θ (below the SOM). Both the oxygen concentrations and depths on isopycnal surfaces were normalized by their standard deviations, to find the modes representing the first- and second-largest amounts of variance (e.g., Von Storch and Zwiers 1999). The first mode in the EOF analysis facilitates comparison of the strength of the relationship between isopycnal depth and oxygen concentration by comparing the first-mode proportion of the variances (and corresponding correlations) among the two isopycnals. After that, we showed where the relationships differed from the first mode as revealed by the second mode and discussed the cause of the relationships. Because the group distributions differed between YDAYs 207–242 (the first period) and YDAYs 243–272 (the second period), we have presented the results of the two periods separately.

i. The first period (YDAYs 207–242)

On each isopycnal surface, the first mode of the EOF indicates that higher oxygen concentrations were frequently observed at shallower depths on the same isopycnal surfaces, where the light and nutrient environment was better for phytoplankton growth (Fig. 9). However, because the difference between the proportions of the first (55%) and second (45%) modes was smaller at the SOM on the 24.0σ_θ isopycnal than that (the proportions of the first and second modes were 63% and 37%, respectively) on the 24.8σ_θ, a clear relationship could not be detected with the EOF. Furthermore, groups 1–6 were not generally aligned with the

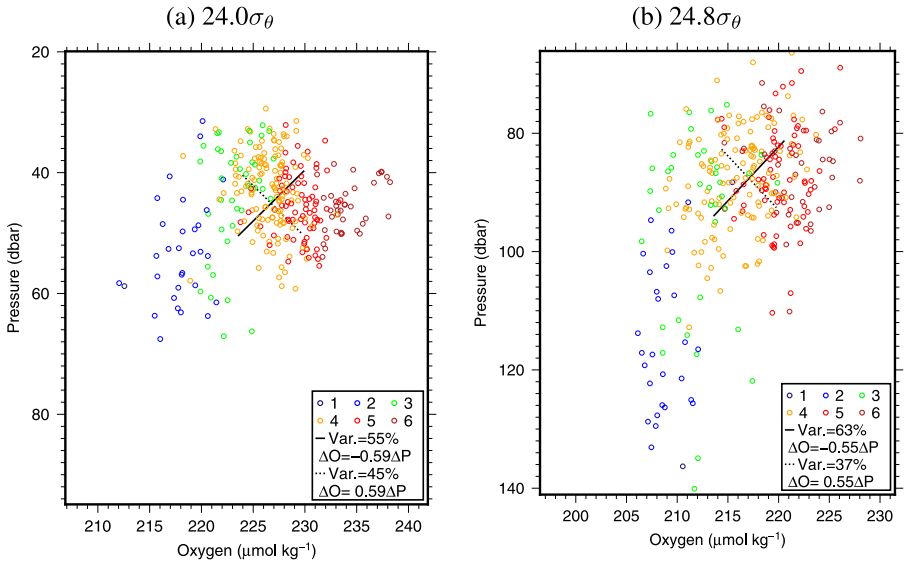

Figure 9. Oxygen and pressure relationships on the (a) 24.0σ_θ and (b) 24.8σ_θ isopycnal surfaces during the first period (YDAYs 207–242). The colors of the groups are the same as those shown in Figure 4. The solid and dotted lines denote the ±1 intervals of the components for the first and second mode of the empirical orthogonal function (EOF), respectively. The proportions of the variances ("Var.") and the linear relationships between pressure (ΔP) and oxygen concentration (ΔO) deviations, which are corresponding to the inclinations of solid and dotted lines, for each mode are also shown in the legends. Note that data for below 110 dbar on the 24.8σ_θ isopycnal surfaces were not used for the EOF analysis because the relationships differed greatly from those at the other depths. σ_θ, potential density; YDAY, time interval in days since January 1, 2011.

first-mode direction, the indication being that isopycnal heaving alone does not explain the changes in oxygen concentrations. This result of smaller first-mode proportion at the SOM was because changes in both light conditions and nutrient concentrations at the SOM were smaller than those below the SOM, as the changes in the isopycnal depths of the SOM were smaller than those below the SOM (Fig. 9), and the nitrate concentrations were low (near oligotrophic conditions) (Fig. 6). The low nutrients may have been caused by the relatively constant favorable light conditions on this isopycnal surface before the observation period. On the other hand, the fact that the first-mode proportions (63%) were large below the SOM (24.8σ_θ; Fig. 9b) suggests the importance of nutrient transport by isopycnal heaving. The relatively constant oxygen concentrations (approximately 210 μmol kg^{-1}) on the 24.8σ_θ surface below 110 dbar were similar to those on the 25.0σ_θ surface (not shown) and reflect the low-light conditions below the euphotic zone. To avoid the strong relationships between isopycnal depths and oxygen concentrations below 110 dbar, the data for below 110 dbar were not used for the EOF calculation on 24.8σ_θ.

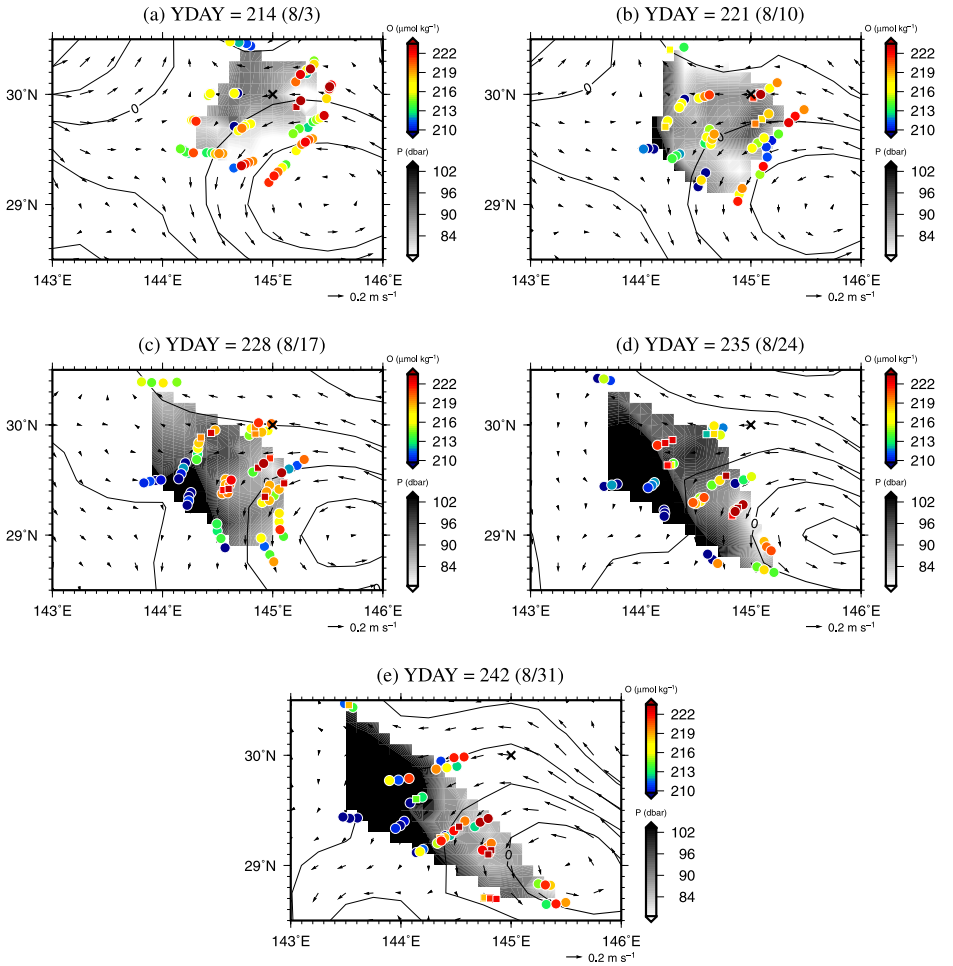

Figure 10. Oxygen (colored circles and squares) and isopycnal depth (gray shade) distribution on the 24.8σ_θ isopycnal (below the SOM and at the bottom of the euphotic zone) around YDAY = 214 (a), YDAY = 221 (b), YDAY = 228 (c), YDAY = 235 (d), and YDAY = 242 (e). The contours show the SSHA (cm). The geostrophic velocity estimated with SSH is shown by vectors. The colored squares denote the high-oxygen water for which the second mode of empirical orthogonal function was >1 (Fig. 9). σ_θ, potential density; SOM, shallow oxygen maximum ; SSHA, sea surface height anomaly; YDAY, time interval in days since January 1, 2011.

As the relationships between the oxygen concentrations and isopycnal surfaces were relatively clear on 24.8σ_θ, to elucidate the spatial patterns corresponding to the first and second modes we examined horizontal maps of the isopycnal depths of the 24.8σ_θ surface superimposed on the oxygen concentrations (Fig. 10). Here, the isopycnal surface depths observed in the profiles within 0.1° × 0.1° for a week were averaged, and then the

horizontal isopycnal depth maps were obtained from the averaged isopycnal depths with linear interpolation. Between YDAYs 211 and 231 (Fig. 10a–c), there was a small-scale disturbances (e.g., see the regions <90 dbar in Fig. 10) in the isopycnal depths along the 0 cm SSHA contour on the shallow isopycnal surface. Relatively high oxygen concentrations were frequently observed around the region with shallower isopycnal surfaces of the small-scale disturbances and along the 0 cm SSHA contour; oxygen concentrations differed more distinctly between the inside and outside of the eddy core, for example, within the 0 cm SSHA contours on YDAYs 214 and 221 (Fig. 10a and b) and within the region of SSHAs lower than 5 cm on YDAYs 235 and 242 (Fig. 10d and e). These patterns suggest that the first mode (Fig. 9b) on $24.8\sigma_\theta$ reflects the oxygen concentration attributable to isopycnal heaving associated with both the eddy-edge disturbances and the eddy core. However, high oxygen concentrations were also observed relatively deep, especially near the region where the horizontal gradient of pressure on the isopycnal surface was large after YDAY 228 (in the region from gray to black for the pressure fields in Fig. 10c–e). Such high oxygen concentrations were associated with the second EOF mode observed around 29.9° N, 144.2° E and 29.4° N, 144.5° E (colored squares in Fig 10c), 29.2° N, 144.8° E (Fig. 10d), and 29.2° N, 144.4° E (Fig. 10e). Because the isodepth lines were not aligned with SSHA contours and crossed the geostrophic velocity vectors, especially near the region where the strong second EOF modes were detected, the high oxygen concentrations in deeper waters might be associated with a downward vertical velocity associated with downgradient flow (we show estimated vertical velocity fields in Section 3e) near the high-gradient regions, where conditions are expected to have been favorable for oxygen production by phytoplankton.

ii. The second period (YDAYs 243–272)

The firstmode proportions and ratios of oxygen concentration deviations to pressure deviations (Fig. 11) were larger than those in the first period (Fig. 9); the first modes show a negative correlation between isopycnal depths and oxygen concentrations, as was the case during the first period. The more distinct relationships (the first-mode EOF) reflect the differences in isopycnal surface depths between inside and outside of the cyclonic eddy; these differences might be maintained for a month or more. Otherwise, the clear relationships were attributable to the distribution of floats, which was relatively sparse along the eddy edge during this period.

Note that during the second period, the mean oxygen concentrations on the $24.0\sigma_\theta$ surface (corresponding to the SOM) were similar to those during the first period (Figs. 9a and 11a) despite the deeper mean isopycnal surface depths ($\approx$60 dbar). This fact suggests that the changes of light conditions were not very important for phytoplankton production on this isopycnal surface, presumably because phytoplankton there were more nutrient limited (see Fig. 6) than light limited.

The clear relationships between the higher oxygen concentrations (red circles) and shallower isopycnal surfaces below the SOM (e.g., $24.8\sigma_\theta$ surface <96 dbar; Fig. 12) indicate the importance of nutrient transport by heaving of isopycnal surfaces in the eddy core.

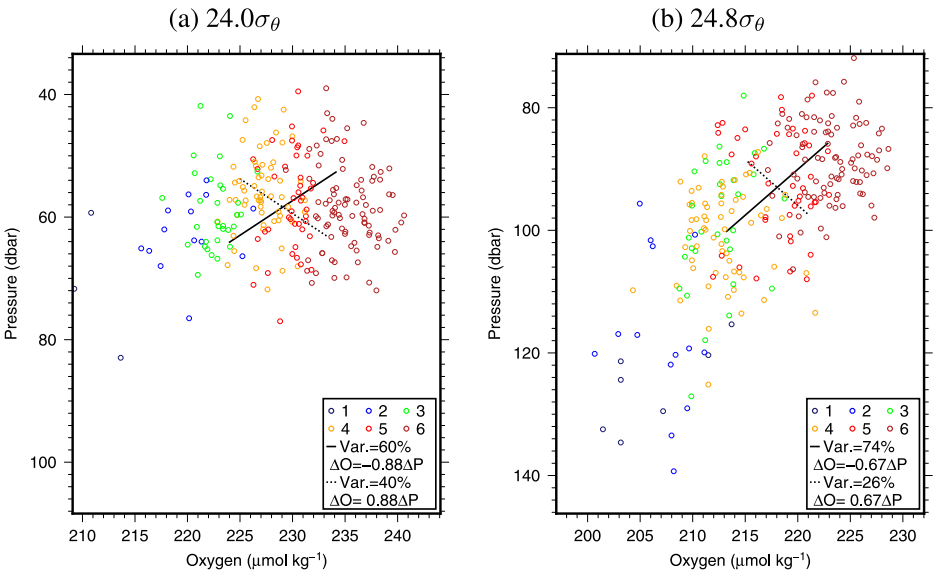

Figure 11. Second period (YDAYs 243–272). See Figure 9 caption for details. σ_θ, potential density; YDAY, time interval in days since January 1, 2011.

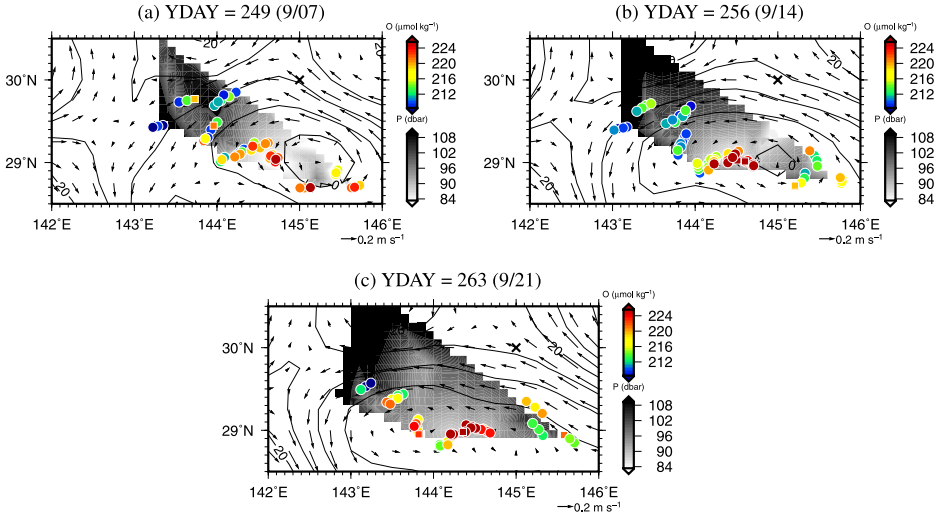

Figure 12. During the second period (YDAYs 243–272), around YDAY = 249 (a), YDAY = 256 (b), and YDAY = 263 (c). See Figure 10 caption for details. YDAY, time interval in days since January 1, 2011.

Whereas the flow (>0.2 m s^{-1}) around the cyclonic eddy became stronger than during the first period, the small-scale disturbances of isopycnal surfaces were unclear around the eddy (e.g., along the 10 cm SSHA contours), and the oxygen increases associated with the second EOF mode in the first period were not observed in the second period.

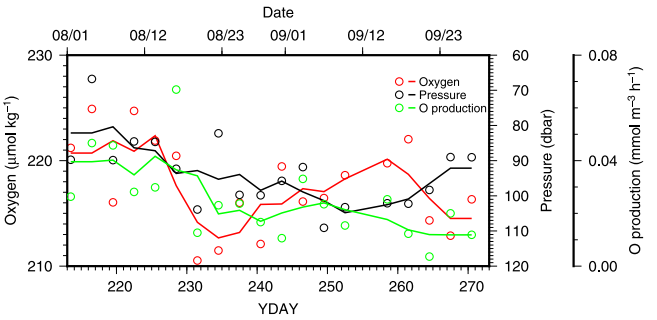

Figure 13. Time series of oxygen (red, left ordinate), isopycnal depths (black, right ordinate), and potential production of oxygen (green, far right ordinate) by the underwater profiling buoy system on the 24.8σ_θ isopycnal. Circles show each cast which was done once every 3 days, and lines show the 9-day running means. σ_θ, potential density.

iii. Comparison with the underwater profiling buoy system

The underwater profiling buoy system, which was located at the northwestern edge of the cyclonic eddy (Part 2), also recorded the high oxygen concentrations on the 24.8σ_θ isopycnal when this surface was both shallow (≈80 dbar from YDAYs 214 to 227) and deep (≈100 dbar from YDAYs 249 to 264) (Fig. 13). In the first mode of the EOF the proportion of the variance and the ratio of the oxygen to the pressure deviations were also estimated to be similar (69% and –0.43 μmol kg^{-1} dbar^{-1}, respectively) to the values recorded with the float array (Figs. 9 and 11). The potential oxygen production rates, which were estimated with a submersible fast-repetition-rate fluorometer (FRRF; Diving Flash, Kimoto Electric, Osaka, Japan; see Part 2), seem to be associated with the depths of the isopycnal surfaces (Fig. 13), which were also shown in Part 2. However, the sampling frequency (every 3 days for 2 months) might be insufficient to demonstrate statistical significance. This relationship suggests that the potential oxygen production rates were strongly affected by the instantaneous changes in the light environment on the isopycnal surfaces attributable to vertical motions, but the oxygen concentration was expected to be related to the time integration of production rate over long periods.

f. Changes in subsurface oxygen and vertical velocity around the cyclonic eddy

Below the SOM, oxygen concentrations tended to be higher on shallower isopycnal surfaces (Figs. 10 and 12). Here, we compare the vertical velocity field (estimation method in Appendix) at 80 m averaged over a week and the oxygen concentrations at the SOM observed 1 week later to elucidate the time-integrated effects of vertical velocity. We assumed that the changes in oxygen concentrations would become apparent quickly after the environmental changes caused by isopycnal heaving, while the water particles were also moving horizontally.

Generally, vertical velocities along eddy edges are associated with horizontal ageostrophic currents and are a part of the ageostrophic secondary circulation (e.g., Calil and Richards 2010). Because the ageostrophic circulation often flattens the front at the eddy edges, vertical velocities in that part of the ageostrophic secondary circulation are related to the fluctuations along the front (not to the SSHA directly), as shown in previous studies (e.g., Martin and Richards 2001). Indeed, the relationships of vertical velocities and SSHA (the pattern correlation was approximately zero) were not clear (Fig. 14). Vertical velocity fields estimated from the ω-equation varied with the locations and shapes of the eddy (Fig. 14). In the first period (YDAYs 207–242), upwelling and downwelling regions alternated around the northwestern region of the cyclonic eddy (Fig. 14a–e); the spatial scales of these upwelling and downwelling regions along the SSHA contours were approximately 20–40 km. For example, upwelling was estimated around 29.5° N, 144.5° E during the weeks centered around YDAYs 228 and 235, and downwelling occurred to the east of the upwelling. During the week centered around YDAY 249, the upwelling region was around 29.3° N, 144.4° E, and the downwelling region was around 29.5° N, 145° E. Note that the spatial scales of upwelling and downwelling (Fig. 14a–e) were similar to the actual changes of isopycnal surface depths (e.g., along the 10 cm SSHA contour in Fig. 10). The estimated vertical velocity could thus qualitatively capture the observed field. In the second period (YDAYs 243–272), the amplitude of the vertical velocity decreased. This reduction was associated with a decrease of the relative vorticity estimated from the SSHA (Fig. 2). The pattern of weak upwelling and downwelling from the west and the center of the eddy, respectively, was associated with the westward propagation and extension of the eddy core (Fig. 2f–h).

The upwelling regions in the northwestern part of the eddy in the first period (around 30° N, 144.2° E in Fig. 14a and 29.3° N, 144.2° E in Fig. 14c and d) and in the center of the eddy in the second period (around 143° E in Fig. 14g and h) seem to be coincident with the profiles with relatively high oxygen concentrations (red circles in Fig. 14). Especially the pattern correlations between oxygen concentrations around SOM ($24.0\sigma_\theta$) and the vertical velocities during YDAYs 228–242 (Fig. 14c and d) were high (0.4 and 0.5, respectively). This was consistent with the speculation from the profiling buoy system data (Fig. 13) that the time-integrated effects of upwelling (rather than the instantaneous ones) can form the high-oxygen regions. Especially around 29.2° N–29.8° N, 144.5° E–144.8° E during YDAYs 228–242 (Fig. 14c and d), when the averaged (temporally integrated) upwelling was coincident with high oxygen concentrations, profiles with high oxygen concentrations were observed simultaneously in both the downwelling and upwelling regions (compare high-oxygen profile circles in Fig. 14c and d with the vertical velocity in Fig. 14d and e). The eddy's counterclockwise flow field transported water containing a high concentration of oxygen to the south on the western edge of the eddy, and local convergence associated with ageostrophic flows in the layers lighter than $24.8\sigma_\theta$ caused downwelling and may have pulled the high-oxygen water into the eddy core (Fig. 14c–e). The fact that the salinity ($\approx$34.76 in Fig. 8) of these high-oxygen waters was similar to that of the eddy (Fig. 8c and

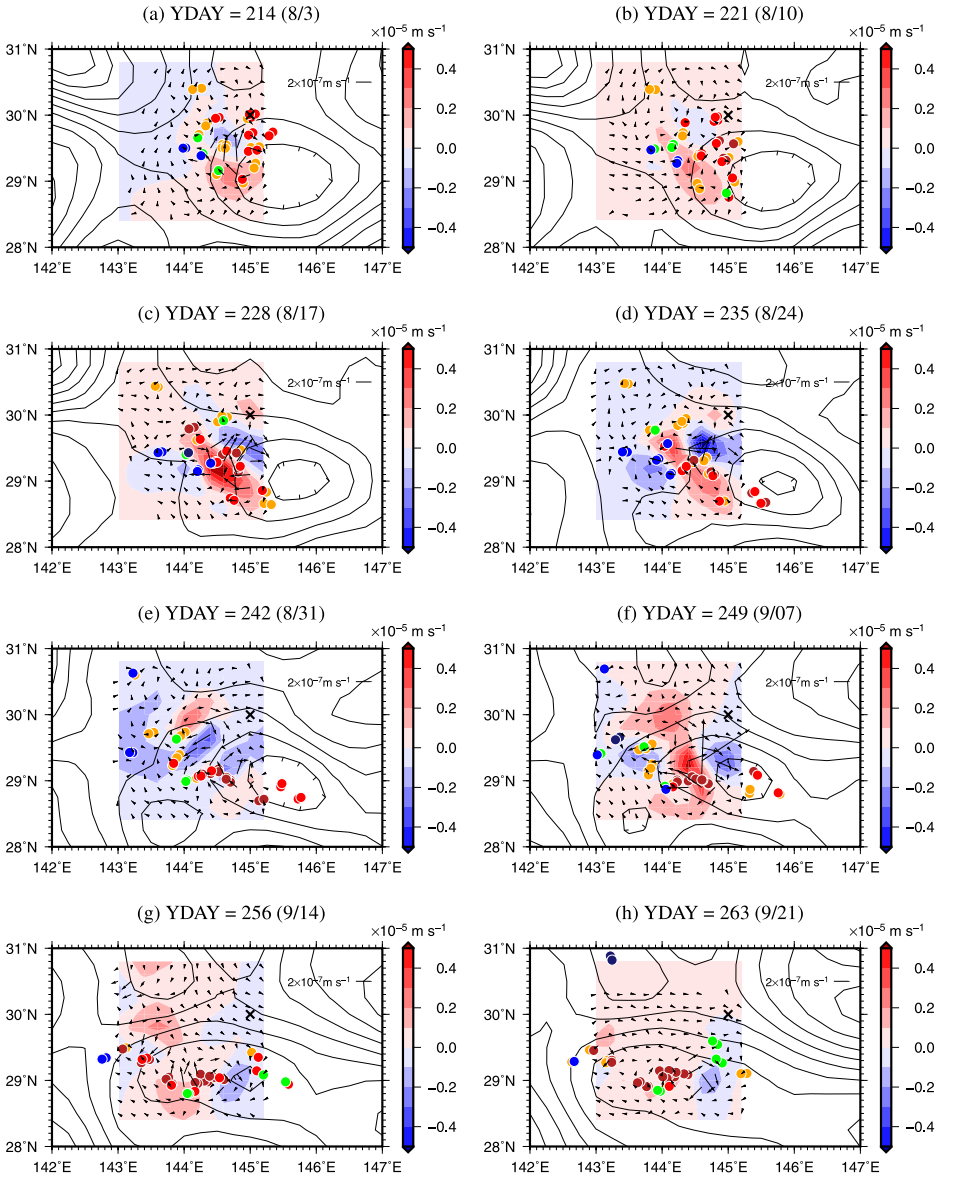

Figure 14. Weekly averaged upward vertical velocity ($\times 10^{-5}$ m s^{-1}) at 80 m (colored shading) around YDAY = 214 (a), YDAY = 221 (b), YDAY = 228 (c), YDAY = 235 (d), YDAY = 242 (e), YDAY = 249 (f), YDAY = 256 (g), and YDAY = 263 (h). Contours and arrows show the SSHA (cm) and ageostrophic horizontal velocity (m s^{-1}), respectively. The black X denotes the location of the S1 mooring. The YDAYs (dates) are the middle dates for the composite period. Colored circles denote the groups (associated with oxygen concentrations around the SOM in Fig. 4) that were observed with in a subsequent week after the period of averaged vertical velocities. SOM, shallow oxygen maximum; SSHA, sea surface height anomaly; YDAY, time interval in days since January 1, 2011.

d) is consistent with the possibility of advection from the edge to the core of the eddy. The fact that these features were common on isopycnal surfaces lighter than the STMW during INBOX observations suggests that the effects of intermittent upwelling and horizontal advection on the distribution of oxygen concentrations around the SOM of cyclonic eddies cannot be ignored.

g. Ocean color around the cyclonic eddy

In the previous section, we have shown that the averaged (temporally integrated) upwelling regions tend to coincide with those with relatively high oxygen concentrations. However, the high chl. *a* concentrations estimated from satellite images did not always coincide with high subsurface oxygen concentrations and upwelling (e.g., see around 29.3° N, 144.2° E in Fig. 14b–d and Fig. 15b–d). Upwelling can contribute to relatively high chl. *a* in satellite images by uplifting subsurface chl. *a* maxima toward the surface (e.g., Killworth et al. 2004) and by producing a good environment for phytoplankton growth by introducing nutrient-rich water into the euphotic zone. Below the mixed layer during our observations, the potential oxygen production rates estimated with data from the underwater profiling buoy system were more clearly related to isopycnal heaving (Fig. 13) than to the surface chl. *a* values (not shown); therefore, the changes in oxygen concentrations might be attributable to changes in the subsurface physical environment rather than to changes in the surface chl. *a*. Note that the surface chl. *a* concentrations were strongly affected by horizontal advection, which was revealed by composite analysis for cyclonic eddies in a previous study (Kouketsu et al. 2015).

4. Discussion

Whereas Calil and Richards (2010) calculated vertical velocities to be as high as 4×10^{-4} m s^{-1} near the Hawaiian Islands, our estimation was much smaller, $\approx 5 \times 10^{-6}$ m s^{-1}. Our float observations captured the high- and low-concentration oxygen patches associated with upwelling and downwelling around the eddy edge. Furthermore, relatively high-oxygen patches were observed near the convergence regions around the edge of the cyclonic eddy and in the upwelling regions. Because ageostrophic secondary circulation around the edge of a cyclonic eddy can generally transport waters across the front from the outside deep layer to the inside shallow layer near the sea surface (e.g., Lapeyre and Klein 2006; Calil and Richards 2010), the relatively high-oxygen water might have been attributable to movement associated with the upwelling of highly active phytoplankton from deep layers to shallow depths. Such events may frequently occur at the edge of an eddy as a result of small-scale disturbances of the vertical velocity, and they may influence the formation of high-oxygen waters in the eddy core. The oxygen production in patches around the eddy edge might be as high as 0.7 μmol kg^{-1} d^{-1} (= 0.03 mmol m^{-3} h^{-1} in Fig. 13), and the spatial (≈40 km) and temporal (≈7 days from the mooring observation) scales of the patches were small.

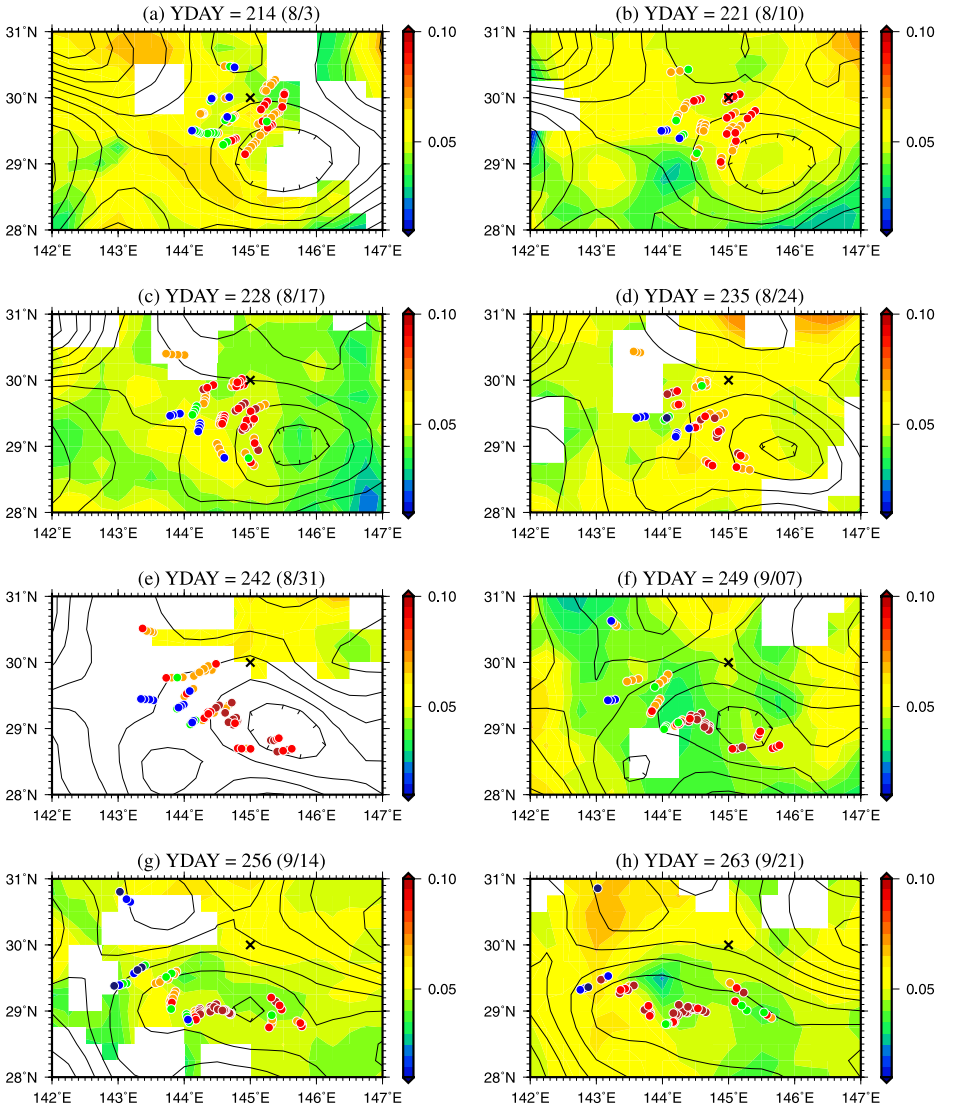

Figure 15. Weekly chlorophyll a (colored shading) from satellite averaged with daily data (McClain, Feldman, and Hooker 2004) around YDAY = 214 (a), YDAY = 221 (b), YDAY = 228 (c), YDAY = 235 (d), YDAY = 242 (e), YDAY = 249 (f), YDAY = 256 (g), and YDAY = 263 (h). Contours show the SSHA (cm). The black X denotes the location of the S1 mooring station. The YDAYs (dates) are the middle dates for the composite period. Colored circles denote the groups in Figure 4, which reflect the oxygen concentrations around the SOM. SOM, shallow oxygen maximum; SSHA, sea surface height anomaly; YDAY, time interval in days since January 1, 2011.

To compare the oxygen changes on the isopycnal surfaces, we calculated the budget of oxygen around the SOM (depths of 50–110 m) near site S1 during the first period (Fig. 16 and equation A6 in Appendix). At first, by assuming that the vertical diffusion of oxygen concentration and nutrient supply from the deeper layers could be neglected, we estimated the oxygen production from the sum of the temporal changes and three-dimensional advection effects $\left(\frac{\partial O}{\partial t} + v \cdot \nabla O\right)$. The temporal variations in the estimated oxygen production (dashed black line in Fig. 16b) were similar to the potential oxygen production rates estimated with the FRRF attached to the mooring buoy (green dots in Fig. 16b), but there was an offset. Although the relatively large potential and estimated oxygen production rates were consistent with the horizontal and temporal oxygen changes on the isopycnal surfaces ($\approx$0.7 μmol kg^{-1} d^{-1}), they were much larger than those estimated from the total mass fluxes into the sediment trap at 200 m (black line in Fig. 16b; Part 2), assuming the Redfield ratio of DO:C (117:170) The estimated oxygen production might be associated with the biological activity changes using in situ nutrients in the euphotic zone, which were transported from the deeper layer before these observations.

On the other hand, the oxygen increases estimated from the sediment trap fluxes were comparable to the sum of the effects of nitrate supplies attributable to vertical diffusion and advection (red dashed line in Fig. 16c), while there were not small differences. Here, oxygen changes by nutrient supply attributable to vertical diffusion (green and dashed green lines with vertical diffusion [K_v] assumed to be 1.0×10^{-5} m^2 s^{-1} and 1.0×10^{-4} m^2 s^{-1}, respectively) were inferred from the fifth term in the right-hand side of equation (A6), and those attributable to vertical advection (orange) were calculated with the fourth term in the right-hand side of equation (A6), assuming the Redfield ratio of DO:N (117:16) and the nitrate profile shown in Figure 6. The effect of vertical diffusion of oxygen (blue and dashed-blue lines for the same K_v values as mentioned previously, respectively) was calculated with the third term in the right-hand side of equation (A6). The carbon export flux to the deeper layers corresponding to the sediment trap fluxes might be associated with such vertical effects rather than with instantaneous productions in the euphotic zone. However, as the advection effects were comparable to the temporal changes (Fig. 16b), estimates of the exact advection effects were needed to determine oxygen production rates based on the residuals of temporal changes and advection effects. Geostrophic velocity estimation may not be exact enough for the detailed budget analysis, even though there were many observation points (Fig. 16a), and ageostrophic advection associated with submesoscale dynamics might be underestimated in this study because of the quasi-geostrophic approximation.

Based on the fact that high nitrate concentrations were observed below the SOM for about a week during the ship observations (Fig. 6), horizontal advection on isopycnal surfaces and changes in the light environment attributable to heaving might play a crucial role in the spatial and temporal changes of oxygen concentrations. However, the oxygen changes at the SOM, where nitrate concentrations were close to 0 (Fig. 6), might be strongly affected

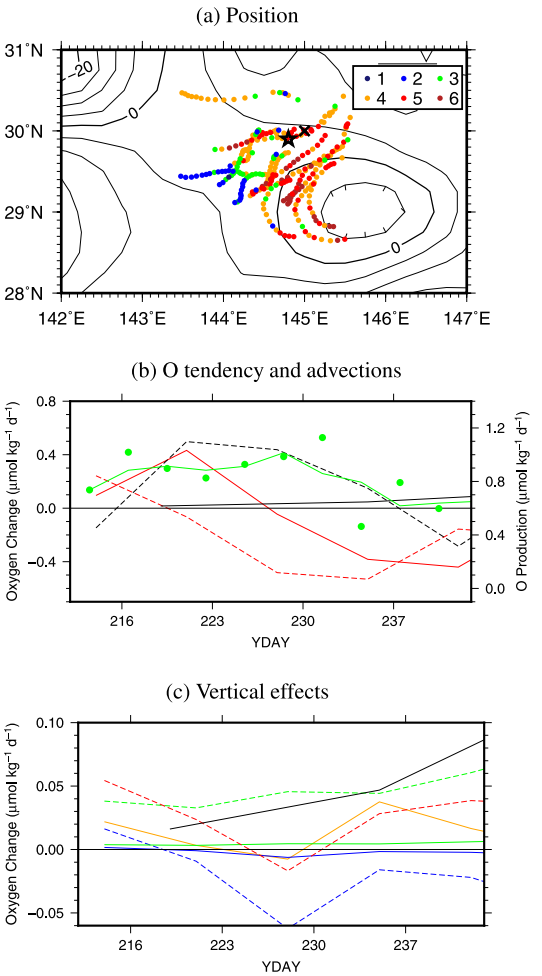

Figure 16. Oxygen budget (μmol kg^{-1} d^{-1}) in the shallow surface oxygen maximum layer near the S1 mooring site during the first period (YDAY 207–242). (a) Distribution of the oxygen profile groups as in Figure 7, but only the observations during the first period are shown, and the black star shows the point (144.8° E, 29.9° N) for which the budget calculation was carried out. (b) Oxygen temporal changes (red line, left ordinate; left-hand side of equation A6) and advection effect (dashed red line, left ordinate; the first and second term in the right-hand side of equation A6) near the SOM (50–110 m). Dashed black line (left ordinate) is the sum of the oxygen temporal changes and advection effect. The solid black line (left ordinate) is the oxygen increase estimated from carbon accumulation in sediment traps, assuming the Redfield ratio of DO:C (117:170). Green circles and lines are potential oxygen production rates (right ordinate) averaged over the SOM and their 9-day running means, respectively (adapted from Fig. 13). (c) Oxygen changes inferred by nutrient supply attributable to vertical diffusion (green solid line with $K_v = 1.0 \times 10^{-5}$ m^2 s^{-1} and dashed line with $K_v = 1.0 \times 10^{-4}$ m^2 s^{-1}; the fifth term in the right-hand side of equation A6) and vertical advection (orange; the fourth term in the right-hand side of equation A6). Blue solid and dashed lines denote vertical diffusion effects, with the diffusion coefficient assumed to be 1.0×10^{-5} m^2 s^{-1} and 1.0×10^{-4} m^2 s^{-1}, respectively (the third term in the right-hand side of equation A6). The dashed red line denotes the sum of the diffusion effects shown by green and blue dashed lines. DO, dissolved oxygen; SOM, shallow oxygen maximum; YDAY, time interval in days since January 1, 2011.

by diapycnal mixing, as discussed in Part 2. Because the higher oxygen concentrations below the SOM were in the groups with the higher oxygen concentration around the SOM (see Fig. 4a), the changes associated with isopycnal heaving below the SOM can also be related to the SOM changes. The upward isopycnal heaving can supply nutrient-rich water below the SOM, and the vertical nitrate differences between at and below the SOM can be large. The stronger vertical nitrate gradient attributable to the isopycnal heaving below the SOM tended to create a relatively large nutrient supply through vertical mixing, as well as advection, and can cause high oxygen concentrations below the SOM. The high oxygen concentrations below the SOM can help to prevent decay of the SOM via diapycnal mixing. At the same time, vertical mixing could transport oxygen downward. To determine the exact contribution of small-scale disturbances to the formation of high oxygen concentrations in an eddy core, it would be necessary to observe in detail the physical fields around an eddy (e.g., horizontal velocity and vertical diffusivity) and nutrient distributions.

As the second-mode proportion in the EOF tended to be larger in the regions downstream of the high-oxygen patches where a large horizontal isopycnal surface gradient and downwelling were estimated, the second mode possibly included the effect of the high-oxygen (low-oxygen) waters, which could have been produced in the small-scale disturbances around the eddy and subsequently advected to the deeper (shallower) isopycnal surfaces. However, short-term changes caused by physical processes such as heaving associated with internal waves and sub-mesoscale advection could also contribute to the second mode because short-term changes attributable to transport might be faster than in situ changes attributable to phytoplankton activity. Although the low-oxygen and relatively shallow isopycnal surface event (YDAY 235 in Fig. 13 and Part 2) may be associated with such very short-term changes, higher frequency observations would be necessary to capture such phenomena.

5. Summary

In this report, we describe in detail the distribution of oxygen at the SOM and at the base of the euphotic zone around a cyclonic eddy during the S1-INBOX float observations. We observed high- and low-oxygen patches with horizontal scales of 20–40 km around the edge of the eddy, as well as relatively high oxygen in the eddy core. The vertical velocity at the base of the euphotic zone alternated between upwelling and downwelling. The upwelling might have contributed to the formation of a patchy oxygen concentration pattern by uplifting relatively nutrient-rich water from deep layers. Water exchanges between the eddy edge and core could have influenced the concentration of oxygen in the core; we suggest that the high-oxygen patches extended into the core. Because the highest oxygen concentrations were observed in the core during YDAYs 243–272, more long-term “eddy pumping effects” could have contributed to the formation of the high oxygen concentrations around SOM in the eddy core. Because of the strong effect

of horizontal advection, the high-oxygen production events around eddy edges must be resolved to evaluate their relative importance with respect to formation of SOM. Observations of velocity fields and nutrient concentrations by a higher-resolution float array would improve this evaluation. Finally, whereas our analysis focused on the cyclonic eddy observed just after deployment, this S1-float data set might also facilitate study of the effects of an anticyclonic mode water eddy (observed after the second period) and wintertime convection.

Acknowledgments. We thank Messrs. Nakajima and Matsuo for technical support of the float observations. We express our appreciation to the captain, crew, and scientists of the MR11-05 cruise for their successful deployment of many floats. The detection of spatial and temporal changes of oxygen was possible because Drs. Uchida and Sato performed quality-control calibration of the sensors. We thank Drs. T. Saino, M. Honda, K. Sasaoka, T. Kobayashi, and S. Hosoda for fruitful discussions. S. Kouketsu was supported by a Grant-in-Aid for Scientific Research on Innovative Areas (grant no. 12024485).

APPENDIX

a. Interpolation

We used a Markov chain Monte Carlo (MCMC) method, which was employed in Kouketsu and Murata (2014), to create gridded data based on 18 float observations of temperature, salinity, pressure, and dissolved oxygen from the surface to 2,000 dbar every other day. In applying the MCMC, we did not assume spatial and temporal length scales, because we wanted to avoid strong constraints imposed by spatial structures, which cannot be easily known in such an experiment. For the MCMC, we assumed the following probability distribution:

$$
\begin{aligned}
&p(y_o;\, y_g, \tau_o) \propto \\
&p(\tau_o) \\
&p(y_g;\, m_g, t_g, \tau_g, \alpha_g)\, p(\tau_g)\, p(\alpha_g) \\
&p(m_g;\, m_{mg}, \tau_{mg}, \alpha_{mg})\, p(\tau_{mg})\, p(\alpha_{mg})\, p(m_{mg}) \\
&p(t_g;\, m_{tg}, \tau_{tg}, \alpha_{tg})\, p(\tau_{tg})\, p(\alpha_{tg})\, p(m_{tg})
\end{aligned}
\tag{A1}
$$

The parameters and probability functions are summarized in Table 1. For $p(y_g;\, t_g, \alpha, x_m, \alpha_{xm})$ and $p(x_m;\, t_m, \alpha_{xm}, x_{mm})$, we used a generalized multivariate conditional autoregressive model (GMCAR) (e.g., Jin, Carlin, and Banerjee 2005). The GMCAR used a Gaussian distribution with a mean calculated from neighbors as the conditional probability function for each grid point. In this way, the gridded data were smoothed with precision (t_g, t_m), but without assuming any particular spatial correlation structure. The data set domain was for 28.5° N–30.7° N, 143.0° E–145.2° E; 0–2,000 m; and time interval in days since January 1, 2011 (YDAY) 212 to YDAY 268, with spatial and temporal intervals of 0.2° and 2 days, respectively. We used the last 1,000 samples of 2,000 MCMC iterations.

Table 1. List of parameters for the Markov Chain Monte Carlo method

Parameter	Meaning
y_o	Observation
y_g	Grid-point value
τ_o	Precision of the probability function for observations
τ_g	Precision of the probability function for a grid-point value
τ_{mg}	Precision of the probability function for a mean value
τ_{tg}	Precision of the probability function for a mean trend
m_g	Temperature and salinity (*TS*) mean value for each level/ within each *TS* segment
t_g	*TS* mean trend for each level/within each *TS* segment
m_{mg}	Mean value for all levels/all segments
m_{tg}	Mean trend for all levels/all segments
$p(y_o; y_g, \tau_o)$	Gaussian with mean of y_g and precision of τ_o
$p(\alpha)$, $p(\alpha_{mg})$, $p(\alpha_{tg})$	Metropolis-Hastings algorithm sampling ([0, 1]) parameters
$p(\tau_o)$, $p(\tau_g)$, $p(\tau_{mg})$, $p(\tau_{tg})$	Gamma distribution parameters
$p(m_{mg})$, $p(m_{tg})$	Gaussian distribution parameters
$p(y_g; m_g, t_g, \tau_g, \alpha)$	Generalized multivariate conditional autor-regressive model parameters
$p(m_g; m_{mg}, t_{mg}, \tau_{mg}, \alpha_{mg})$	
$p(t_g; m_{tg}, \tau_{tg}, \alpha_{tg})$	

b. Diagnosis of vertical motions and oxygen budget

We calculated geostrophic velocity fields relative to a reference level depth of 2,000 m based on the gridded data using the MCMC method; the Ekman current was determined on the assumption that the typical depth (e-folding scale) of the Ekman layer was 50 m. Rossby numbers were calculated to be 0.02–0.04 with typical velocity of 0.3 m s^{-1} and a horizontal scale of 100–200 km (e.g., Fig. 10). Thus, assuming quasi-geostrophic balance, we simply estimated vertical motions with the ω-equation (e.g., Holton 1992; Rudnick 1996; Martin and Richards 2001):

$$N^2\nabla^2\omega + f^2\frac{\partial^2\omega}{\partial Z^2} = 2\nabla\cdot\mathrm{Q} + \beta f\frac{\partial v_g}{\partial z}, \tag{A2}$$

where N is the buoyancy frequency, ω is the vertical velocity, f is the Coriolis parameter, β is the meridional gradient of f, and **Q** is the vector defined as

$$\mathrm{Q} = (Q_x, Q_y) = g/\rho_o\left(\partial v_g/\partial x\cdot\nabla\rho, \partial v_g/\partial y\cdot\nabla\rho\right), \tag{A3}$$

where g is the acceleration of gravity, ρ is the potential density, and v_g is the geostrophic velocity. From the estimated vertical velocity, we can also obtain ageostrophic velocities (u_a, v_a) with the following equations:

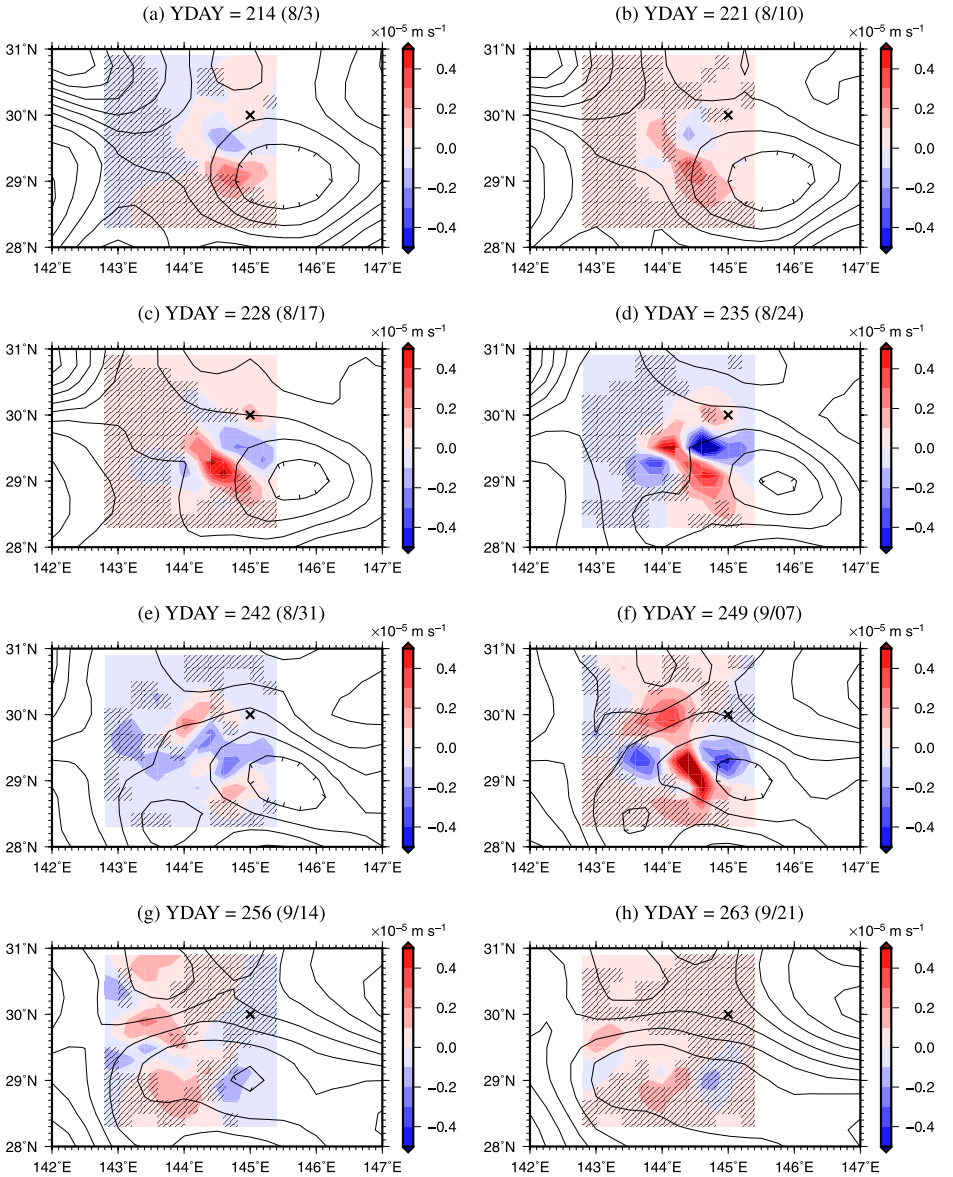

Figure A1. Weekly averaged upward vertical velocity ($\times 10^{-5}$ m^2 s^{-1}) at 80 m (colored shading; same as Fig. 14) around YDAY = 214 (a), YDAY = 221 (b), YDAY = 228 (c), YDAY = 235 (d), YDAY = 242 (e), YDAY = 249 (f), YDAY = 256 (g), and YDAY = 263 (h). The hatched areas show that estimated upwelling or downwelling are insignificant at 95% confidence level. Contours show the SSHA (cm). The black X denotes the location of the S1 mooring. The YDAYs (dates) are the middle dates for the composite period. SSHA, sea surface height anomaly; YDAY, time interval in days since January 1, 2011.

$$\frac{\partial}{\partial x}(N^2\omega) - f^2\frac{\partial u_a}{\partial z} = 2Q_x \tag{A4}$$

$$\frac{\partial}{\partial y}(N^2\omega) - f^2\frac{\partial u_a}{\partial z} = 2Q_y. \tag{A5}$$

For this estimation, we used the ω-equation with instantaneous, three-dimensional stratification structures gridded every other day. The boundary conditions were similar to those in a previous study (Rudnick 1996). The estimated vertical motions were consistent with the instantaneous vertical stratification and geostrophic velocity, whereas observed changes of density with time were not always consistent with the vertical motions. To solve equation (A2), we assumed the vertical velocity to be zero at the surface and horizontal and vertical gradients of the vertical velocity to be zero at the lateral and bottom (at a depth of 2,000 m) boundaries, respectively, of the gridded data. The vertical velocity fields were calculated with 1,000 subsample stratification structures, which were obtained by the MCMC methods described previously. Based on 95% confidence levels calculated from 1,000 weekly averaged velocity fields at 80 m depths, the estimated upwelling and downwelling patterns were significant in the areas focused on in this study (Fig. A1).

By using the three-dimensional velocity field (v), we calculated the oxygen (O) budget with the following equation:

$$\frac{\partial O}{\partial t} = -v\cdot\nabla O + K_v\frac{\partial^2 O}{\partial Z^2} + \gamma_{O:N}\omega\frac{\partial Ni}{\partial z} - \gamma_{O:N}K_v\frac{\partial^2 Ni}{\partial z^2}, \tag{A6}$$

where K_v is vertical diffusivity, $\gamma_{O:N}$ is the Redfield ratio between oxygen and nitrate, and Ni is the nitrate concentration. The temporal changes in oxygen on the left-hand side of equation (A6) and the oxygen advection effects of the first and second terms on the right-hand side were evaluated from the gridded data. Because the mixedlayer depths were shallower than the shallow oxygen maximum (SOM) depths (approximately 40 m) during the analysis periods (Part 1), we assumed that air-sea exchange would not directly affect the SOM, and the vertical diffusion of oxygen (the third term on the right-hand side of equation A6) was also estimated with the gridded data, assuming K_v to equal either 1.0×10^{-5} or 1.0×10^{-4} m^2 s^{-1}, as the lower and upper bounds, respectively, estimated from measurements made at moorings below the mixed layer (Part 2). The nutrient supplies attributable to heaving and vertical diffusion (the fourth and fifth terms, respectively, on the right-hand side of equation A6) were estimated by assuming a vertical profile averaged over the shipboard measurements during cruise MR11-05 (Fig. 6).

REFERENCES

Bibby, T. S., M. Y. Gorbunov, K. W. Wyman, and P. G. Falkowski. 2008. Photosynthetic community responses to upwelling in mesoscale eddies in the subtropical North Atlantic and Pacific Oceans. Deep Sea Res., Part II, *55*(10–13), 1310–1320. doi: 10.1016/j.dsr2.2008.01.014

Calil, P. H. R., and K. J. Richards. 2010. Transient upwelling hot spots in the oligotrophic North Pacific. J. Geophys. Res.: Oceans, *115*, C02003. doi: 10.1029/2009JC005360

Chelton, D. B., P. Gaube, M. G. Schlax, J. J. Early, and R. M. Samelson. 2011. The influence of nonlinear mesoscale eddies on near-surface oceanic chlorophyll. Science, *334*(6054), 328–332. doi: 10.1126/science.1208897

Claustre, H., J. Bishop, E. Boss, S. Bernard, J. F. Berthon, C. Coatanoan, K. Johnson, et al. 2010. Bio-optical profiling floats as new observational tools for biogeochemical and ecosystem studies: Potential synergies with ocean color remote sensing, *in* Proceedings of OceanObs'09: Sustained Ocean Observations and Information for Society, Vol. 2, Venice, Italy, 21–25 September 2009, J. Hall, D. E. Harrison, and D. Stammer, eds. ESA Publication, WPP-306. Rome: European Space Agency. doi: 10.5270/OceanObs09.cwp.17

Gruber, N., S. C. Doney, S. R. Emerson, D. Gilbert, T. Kobayashi, A. Körtzinger, G. C. Johnson, K. S. Johnson, S. C. Riser, and O. Ulloa. 2007. The Argo-Oxygen program, *in* Supporting Documents for the 8th Meeting of the International Argo Steering Team, Paris, France, March 6–9, 2007. Plouzane, France: Argo Information Center, 40–99.

Holton, J. R. 1992. An Introduction to Dynamic Meteorology. San Diego, CA: Academic Press, 511 pp.

Inoue, R., M. Honda, T. Fujiki, K. Matsumoto, S. Kouketsu, T. Suga, and T. Saino. 2016. Western North Pacific Integrated Physical-Biogeochemical Ocean Observation Experiment (INBOX): Part 2. Biogeochemical responses to eddies and typhoons revealed from S1 mooring and shipboard measurements. J. Mar. Res., *74*(2), 71–99.

Inoue, R., T. Suga, S. Kouketsu, T. Kita, S. Hosoda, T. Kobayashi, K. Sato, H. Nakajima, and T. Kawano. 2016. Western North Pacific Integrated Physical-Biogeochemical Ocean Observation Experiment (INBOX): Part 1. Specifications and chronology of the S1-INBOX floats. J. Mar. Res., *74*(2), 43–69.

Jenkins, W. J., and J. C. Goldman, 1985. Seasonal oxygen cycling and primary production in the Sargasso Sea. J. Mar. Res., *43*(2), 465–491. doi: 10.1357/002224085788438702

Jin, X., B. P. Carlin, and S. Banerjee. 2005. Generalized hierarchical multivariate CAR models for areal data. Biometrics, *61*(4), 950–961. doi: 10.1111/j.1541-0420.2005.00359.x

Killworth, P. D., P. Cipollini, B. M. Uz, and J. R. Blundell. 2004. Physical and biological mechanisms for planetary waves observed in satellite-derived chlorophyll. J. Geophys. Res. Oceans, *109*, C07002. doi: 10.1029/2003JC001768

Kouketsu, S., H. Kaneko, T. Okunishi, K. Sasaoka, S. Itoh, R. Inoue, and H. Ueno. 2015. Mesoscale eddy effects on temporal variability of surface chlorophyll *a* in the Kuroshio Extension. J. Oceanogr. doi: 10.1007/s10872-015-0286-4

Kouketsu, S., and A. M. Murata. 2014. Detecting decadal scale increases in anthropogenic CO_2 in the ocean. Geophys. Res. Lett., *41*(13), 4594–4600. doi: 10.1002/2014GL060516

Lapeyre, G., and P. Klein. 2006. Dynamics of the upper oceanic layers in terms of surface quasi-geostrophy theory. J. Phys. Oceanogr., *36*(2), 165–176. doi: 10.1175/JPO2840.1

Ledwell, J. R., D. J. McGillicuddy Jr., and L. A. Anderson 2008. Nutrient flux into an intense deep chlorophyll layer in a mode-water eddy. Deep Sea Res. Part II, *55*(10–13) 1139–1160. doi: 10.1016/j.dsr2.2008.02.005

Lévy, M., P. Klein, and A.-M. Treguier 2001. Impact of sub-mesoscale physics on production and subduction of phytoplankton in an oligotrophic regime. J. Mar. Res., *59*(4), 535–565. doi: 10.1357/002224001762842181

Martin, A. P., and K. J. Richards. 2001. Mechanisms for vertical nutrient transport within a North Atlantic mesoscale eddy. Deep Sea Res., Part II, *48*(4–5), 757–773. doi: 10.1016/S0967-0645(00)00096-5

McClain, C. R., G. C. Feldman, and S. B. Hooker. 2004. An overview of the SeaWiFS project and strategies for producing a climate research quality global ocean bio-optical time series. Deep Sea Res., Part II, *51*(1–3), 5–42. doi: 10.1016/j.dsr2.2003.11.001

McGillicuddy, D. J., Jr., R. Johnson, D. A. Siegel, A. F. Michaels, N. R. Bates, and A. H. Knap. 1999. Mesoscale variations of biogeochemical properties in the Sargasso Sea. J. Geophys. Res.: Oceans, *104*(C6), 13381–13394. doi: 10.1029/1999JC900021

McGillicuddy, D. J., Jr., A. R. Robinson, D. A. Siegel, H. W. Jannasch, R. Johnson, T. D. Dickey, J. McNeil, A. F. Michaels, and A. H. Knap. 1998. Influence of mesoscale eddies on new production in the Sargasso Sea. *Nature*, *394*(6690), 263–266. doi: 10.1038/28367

Morel, A., and J.-F. Berthon. 1989. Surface pigments, algal biomass profiles, and potential production of the euphotic layer: Relationships reinvestigated in view of remote-sensing applications. Limnol. Oceanogr., *38*(8), 1545–1562. doi: 10.4319/lo.1989.34.8.1545

Qiu, B., P. Hacker, S. Chen, K. A. Donohue, D. R. Watts, H. Mitsudera, N. G. Hogg, and S. R. Jayne. 2006. Observations of the subtropical mode water evolution from the Kuroshio Extension System Study. J. Phys. Oceanogr., *36*(3), 457–473. doi: 10.1175/JPO2849.1

Rudnick, D. L. 1996. Intensive surveys of the Azores Front: 2. Inferring the geostrophic and vertical velocity fields. J. Geophys. Res.: Oceans, *101*(C7), 16291–16303. doi: 10.1029/96JC01144

Sarmiento, J. L., G. Thiele, R. M. Key, and W. S. Moore. 1990. Oxygen and nitrate new production and remineralization in the North Atlantic subtropical gyre. J. Geophys. Res.: Oceans, *95*(C10), 18303–18315. doi: 10.1029/JC095iC10p18303

Siegel, D. A., P. Peterson, D. J. McGillicuddy Jr., S. Maritorena, and N. B. Nelson. 2011. Bio-optical footprints created by mesoscale eddies in the Sargasso Sea. Geophys. Res. Lett., *38*, L13608. doi: 10.1029/2011GL047660

Spitzer, W. S., and W. J. Jenkins. 1989. Rates of vertical mixing, gas exchange and new production: Estimates from seasonal gas cycles in the upper ocean near Bermuda. J. Mar. Res., *47*(1), 169–196. doi: 10.1357/002224089785076370

Suga, T., Y. Takei, and K. Hanawa. 1997. Thermostad distribution in the North Pacific subtropical gyre: The Central Mode Water and the Subtropical Mode Water. J. Phys. Oceanogr., *27*(1), 140–152. doi: 10.1175/1520-0485(1997)027<0140:TDITNP>2.0.CO;2

Sukigara, C., T. Suga, T. Saino, K. Toyama, D. Yanagimoto, K. Hanawa, and N. Shikama. 2011. Biogeochemical evidence of large diapycnal diffusivity associated with the subtropical mode water of the North Pacific. J. Oceanogr., *67*(1), 77–85. doi: 10.1007/s10872-011-0008-5

Sweeney, E. N., D. J. McGillicuddy Jr., and K. O. Buesseler. 2003. Biogeochemical impacts due to mesoscale eddy activity in the Sargasso Sea as measured at the Bermuda Atlantic Time-series Study (BATS). Deep Sea Res., Part II, *50*(22–26), 3017–3039. doi: 10.1016/j.dsr2.2003.07.008

Uchida, H., T. Kawano, I. Kaneko, and M. Fukasawa. 2008. In situ calibration of optode-based oxygen sensors. J. Atmos. Oceanic Technol., *25*(12), 2271–2281. doi: 10.1175/2008JTECHO549.1

Von Storch, H., and F. W. Zwiers. 1999. Statistical Analysis in Climate Research. Cambridge: Cambridge University Press, 484 pp.

Ward, J. H., Jr. 1963. Hierarchical grouping to optimize an objective function. J. Am. Stat. Assoc., *58*(301), 236–244. doi: 10.1080/01621459.1963.10500845

Received: *14 November 2013*; revised: *11 December 2015*.